Research Article

Shuguang Chen, Hanjun Gao*, Minghui Lin, Shaofeng Wu, and Qiong Wu

Research on process optimization and rapid prediction method of thermal vibration stress relief for 2219 aluminum alloy rings

https://doi.org/10.1515/rams-2022-0028
received January 10, 2022; accepted February 23, 2022

Abstract: 2219 aluminum alloy rings are important part of liquid cryogenic rocket fuel tanks. Residual stress is inevitably introduced in the forming process of the rings due to the nonlinear thermomechanical coupling conditions, which will affect its mechanical properties, fatigue properties, corrosion resistance, and dimensional stability. Thermal vibratory stress relief (TVSR) has great potential in reducing residual stress, and process optimization of TVSR is necessary to further improve its application, but it is rarely reported. In this study, process optimization of roll formed 2219 aluminum alloy rings is conducted. The influence of vibration amplitude, vibration time, vibration frequency, heating time, holding time, and cooling time on TVSR treatment are investigated. Results show that the maximum equivalent residual stress of 2219 aluminum alloy rings can be reduced by 93.6% after optimized TVSR treatment. With the increase in vibration time, heating time, holding time, and cooling time, the maximum equivalent stress decreases. However, the increase in the vibration amplitude results in an increase in the maximum equivalent stress. Further, a genetically optimized artificial neural network intelligent optimization algorithm is applied to quickly predict the TVSR effect of 2219 aluminum alloy rings.

Keywords: 2219 aluminum alloy, thermal vibration stress relief, process optimization, genetically optimized neural networks

1 Introduction

As a heat treatable precipitation hardening Al-Cu alloy, 2219 aluminum alloy is considered to be one of the most promising materials in the aerospace industry owing to its light weight, excellent stress corrosion resistance [1], weldability [2,3], and good mechanical properties over a wide temperature range from −250 to 250°C [4,5]. A typical application of 2219 aluminum alloy is in the liquid cryogenic rocket fuel tanks, whose top and bottom covers are composed of 2219 aluminum alloy, and transition rings. The manufacturing methods of aluminum alloy rings mainly include die-forging forming, bending and welding forming, and ring rolling forming [6]. The ring rolling has high forming accuracy and good mechanical properties, and has received extensive attention in the industry in recent years [7].

The ring rolling forming process of aluminum alloy involves material nonlinearity and boundary conditions (such as temperature and load) nonlinearity. Under the nonlinear thermomechanical coupling conditions, residual stresses will inevitably be generated [8,9]. During the service process of the rings, the residual stresses will gradually release, resulting in deformation of the ring and loss of shape accuracy [10–12]. In general, residual stresses affect the mechanical properties, fatigue properties, corrosion resistance, and dimensional stability of high-performance ring parts [13]. Large amplitude and uneven distribution seriously affect the manufacturing accuracy and service reliability of rolled rings. In addition, aluminum alloys usually needs to be machined into thin-walled parts in order to meet the needs of aerospace,

* **Corresponding author: Hanjun Gao,** State Key Laboratory of Virtual Reality Technology and Systems, School of Mechanical Engineering and Automation, Beihang University, Beijing, 100191, China; Jingdezhen Research Institute of Beihang University, Jingdezhen, 333000, China, e-mail: hjgao@buaa.edu.cn
Shuguang Chen, Minghui Lin, Qiong Wu: State Key Laboratory of Virtual Reality Technology and Systems, School of Mechanical Engineering and Automation, Beihang University, Beijing, 100191, China; Jingdezhen Research Institute of Beihang University, Jingdezhen, 333000, China
Shaofeng Wu: State Key Laboratory of Virtual Reality Technology and Systems, School of Mechanical Engineering and Automation, Beihang University, Beijing, 100191, China; Key Laboratory of Advanced Manufacturing Technology, Beijing University of Technology, Beijing, 100124, China

and the material removal rate in this process can be as high as 95% [14]. During the machining process, the original residual stress balance state is broken as the material is removed, a new self-equilibrating residual stress field forms within the remaining material with the appearance of warping, torsion, and other deformation phenomena [15]. The residual stress of the blank is one of the important influencing factors of machining deformation [10,11].

In recent years, some meaningful studies in stress relief and homogenization techniques have been conducted. Common stress relief methods include thermal stress relief (TSR) and vibration stress relief (VSR), and thermal vibratory stress relief (TVSR). Tanner and Robinson [16] reported that the residual stress amplitude of aluminum alloy 2014 forging greatly reduced after TSR treatment at 170°C per 12 h. Williams et al. [17] investigated TSR treatment (700°C per 12 h) on residual stress in additive manufacturing 316L stainless steel, and the result showed that the peak residual stress reduced by around 10% in the vertical sample and 40% in the horizontal sample. In order to reduce surface residual stress, Fredj and Sidhom [18] conducted TSR treatment on AISI304 stainless steel. Dong et al. [19] reported that the residual stress of cylindrical welded component is reduced by about 50% after 20 min of VSR treatment. Zhang et al. [20] observed that the average stress relief ratio reached 53% in welded 6082 aluminum alloy plates after ultrasonic VSR treatment. Qu et al. [21] performed VSR treatment on TA15 titanium alloy thick plates, and the results showed that the surface residual stress was reduced by nearly 60%. Wang et al. [22] studied residual stress relaxation and the texture evolution of cold-rolled AZ31 Mg alloys using the VSR technique. Zhang et al. [23] developed an elastic-plastic finite element (FE) model to study the VSR parameters of 304 stainless steel cold-rolled strip.

Compared with TSR and VSR, TVSR has obvious advantages due to higher efficiency and better effect [24,25]. Lv and Zhang [24] found that the stress relief ratio of TVSR is 42.5% higher than that of VSR. Chen et al. [25] reported that TSR treatment effectively reduced the residual stress of welded 2219 aluminum alloys in the direction perpendicular to the weld, TVSR treatment has more advantages in both longitudinal and transversal directions. Li et al. [26] proposed that higher vibration amplitude and temperature are beneficial to reduce residual stress in 50 mm thick DH36 steel welded plates. Wu et al. [27] compared the effect of TVSR treatment with different heating time on 2219 aluminum alloy. Xu et al. [28] conducted TVSR treatment on a thin-walled 7075 aluminum alloy to control the machining deformation, the results show that the maximum deformation decreased by 58.28% compared to the one without any treatment. The residual stress of SiCp/Al composites can be reduced by more than 70% at a temperature of 185°C and a vibration frequency of 56 Hz [29]. Gao et al. [30] analyzed and summarized the stress relief mechanism of TVSR, and proposed a FE modeling method using the creep equation and temperature-dependent thermophysical parameters to simulate TVSR process, the simulation and experimental results are in good agreement. A FE model for simulating the heat treatment process was established using a similar method by Baere et al. [31].

From the above studies, it can be found that TVSR has great potential and application value in reducing the residual stress. TVSR contains many process conditions as it is a coupling method of TSR and VSR. The process optimization of TVSR is very necessary to further improve its application, but it is rarely reported, which may due to the cost and time consumption of the optimization process. In this study, TVSR process optimization of roll formed 2219 aluminum alloy rings is conducted. The influence of vibration amplitude, vibration time, vibration frequency, heating time, holding time, and cooling time on TVSR treatment are investigated. Further, a genetically optimized artificial neural network intelligent algorithm is applied in order to improve the prediction efficiency of TVSR.

2 Materials and methods

2.1 Specimens and TVSR processes

The 2219 aluminum alloy rings used in this article are produced by Shanghai Xijie Metal Products Co., Ltd (Shanghai, China). As shown in Figure 1, the outer diameter of the ring is 450 mm, inner diameter is 366 mm, and the height is 105 mm. The chemical compositions of 2219 aluminum alloys are shown in Table 1. The general processes for TVSR treatment of aluminum alloy are also given in Figure 1. It can be described as: first the sample is heated to a certain temperature, then subjected to vibration with heat preservation, and after holding for a period of time, it is cooled to room temperature.

2.2 FE simulations for TVSR

The general modeling and analysis flow of TVSR is shown in Figure 2, and the entire analysis is conducted in the FE

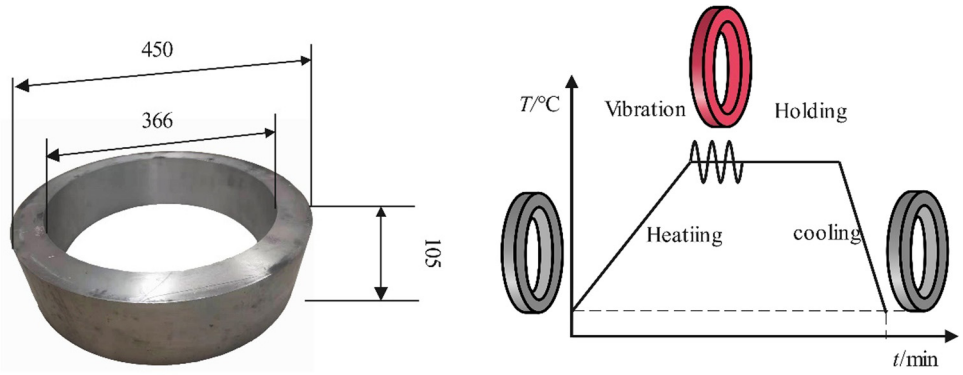

Figure 1: The 2219 aluminum alloy ring and general TVSR processes.

Table 1: Chemical composition of 2219 aluminum alloy (%)

Cu	Mg	Mn	Fe	Si	Zn	Ti	Zr	V	Al
6.227	0.005	0.243	0.142	0.056	0.009	0.039	0.179	0.087	The rest

analysis software ANSYS. The ring is modeled according to the actual size which is given in Figure 1, and eight nodes element Solid185 is selected for meshing as the element can be used for analysis of plasticity, superelasticity, creep, and large deformation. In order to limit the rigid body displacement of the workpiece in three directions and ensure the convergence of the calculation, spring elements Combin14 with a smaller stiffness are spread on the surface nodes of the ring, and the stiffness is 10^{-4} mm·N^{-1}. Before the TVSR numerical simulations, a modal analysis is required to obtain the natural frequencies and modes of the 2219 aluminum alloy ring. We can find that the 7th-order natural frequency of the ring is 619.32 Hz. The relative total deformation of the 7th order is extracted, and it can be seen that the ring vibration is symmetrical. Vibration in TVSR simulation is imposed by nodal displacement, node displacement X can be described as equation (1):

$$X = p\{u_0\} \sin(2\pi ft), \tag{1}$$

where p is a scale factor, $\{u_0\}$ is the node relative total displacement of the 7th-order mode on the upper surface of the ring, f is the 7th-order natural frequency of the ring, and t is the time.

After completing the modal analysis of the ring, the analysis type needs to be converted to transient analysis. The initial residual stress of the 2219 aluminum alloy ring is assigned to the model by the "Inistate" command in ANSYS. The initial residual stress of the 2219 aluminum alloy ring is measured by a drilling method equipment. The schematic of the measurement system and the locations of the residual stress measurement points are shown in Figure 3. When the residual stress measurements are conducted, first, the strain gauges are glued to the polished measurement points and then connected with strain recorder. Next the ring is fixed and the drilling process can be carried out. The residual stress can be calculated from the measured strain variation during the drilling process in the stress analysis interface. Eight points of 2219 ring are measured, the measuring depths of each point are 0.1, 0.2, 0.3, 0.4, 0.5, 0.6, 0.7, 0.8, 0.9, and 1 mm.

The measurement results of the initial residual stress at different depths and directions of the eight measurement points of the 2219 aluminum alloy ring are shown in Figure 4. The more regular the octagon drawn by the residual stresses of eight measuring points, the more uniform the residual stress distribution. On the contrary, the uniformity of the residual stress distribution of the ring is worse. It can be seen that within 1 mm from the outer surface of the 2219 aluminum alloy ring, there are "sharp corners" in the radar images of the residual stress distribution of the eight test points in different directions. Compared with the radial and hoop directions, the residual stress in the shear direction looks more uniform. This may be due to the quenching treatment of the ring, which introduced high amplitude and uneven residual stress during the rapid cooling process.

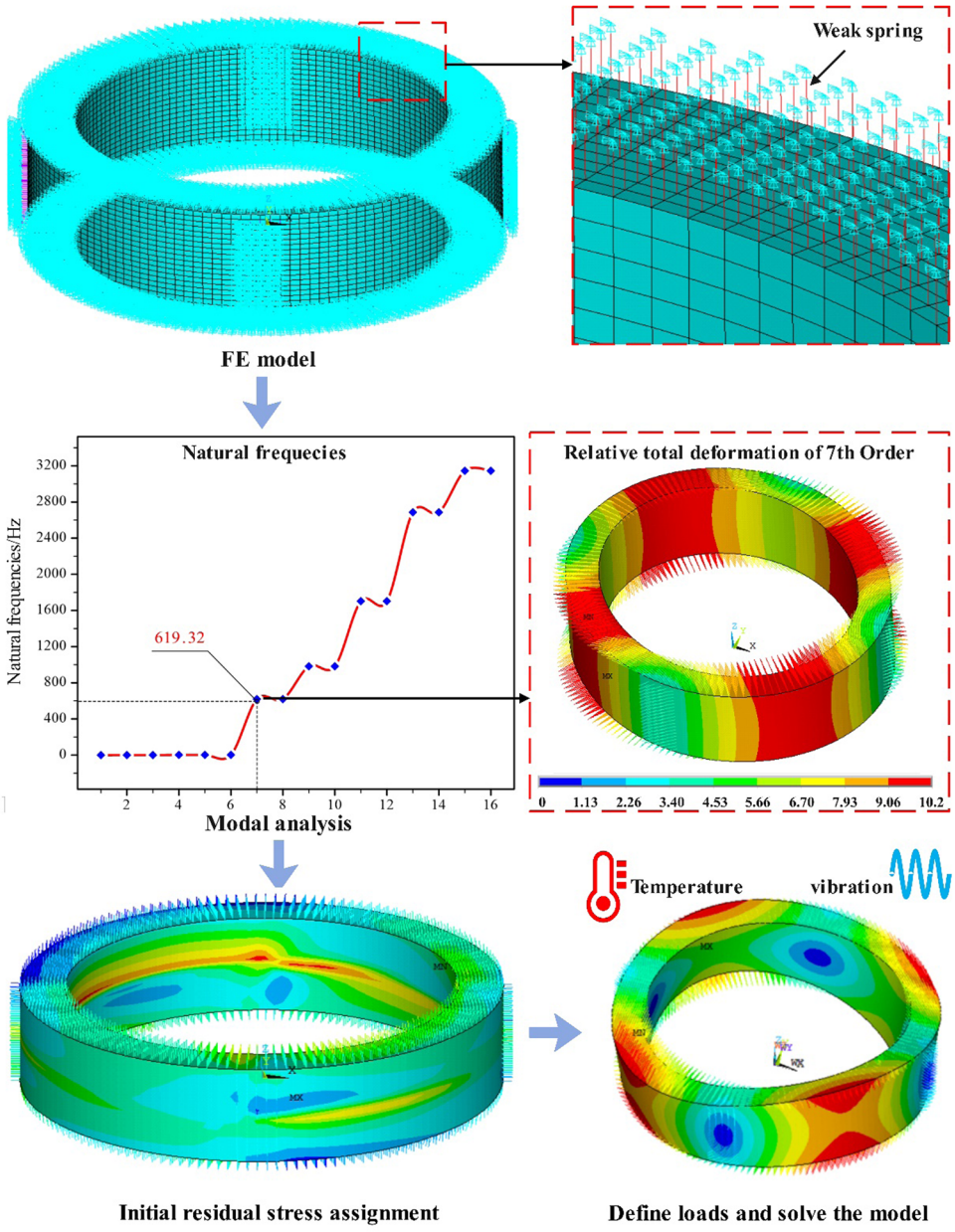

Figure 2: General modeling and analysis flow of TVSR.

In the TVSR process, the peak value of residual stress decreases and the distribution is more uniform. Stress relaxation plays an important role in reducing residual stress, in order to accurately describe the stress in the TVSR process, constitutive equations that reflect the stress relaxation behavior must be included in the FE model. Stress relaxation is another manifestation of the creep phenomenon [32,33]. Therefore, creep equation is adopted in many studies to describe the stress relaxation [34–36]. In this study, the stress relaxation behavior in FE simulations are described by the Norton creep equation [37] described as equation (2).

$$\dot{\varepsilon}_c = C_1 \sigma^{C_2} \varepsilon^{C_2} e^{-C_4/T}, \tag{2}$$

where $\dot{\varepsilon}_c$ is the creep strain rate, σ is the stress, ε is the strain, T is the temperature, and C_1, C_2, C_3, and C_4 are constant coefficients and can be determined by stress relaxation tests. Stress relaxation tests are conducted using RD-50 electronic creep endurance testing machine produced by Changchun Kexin Instrument Co., Ltd (Changchun, China). According to the stress measurement results of the 2219 aluminum alloy ring, stress relaxation tests are carried out under the stress conditions of 50, 150, 250, and 350 MPa, at a temperature of 175°C and a holding time of 18 h. The results of stress relaxation

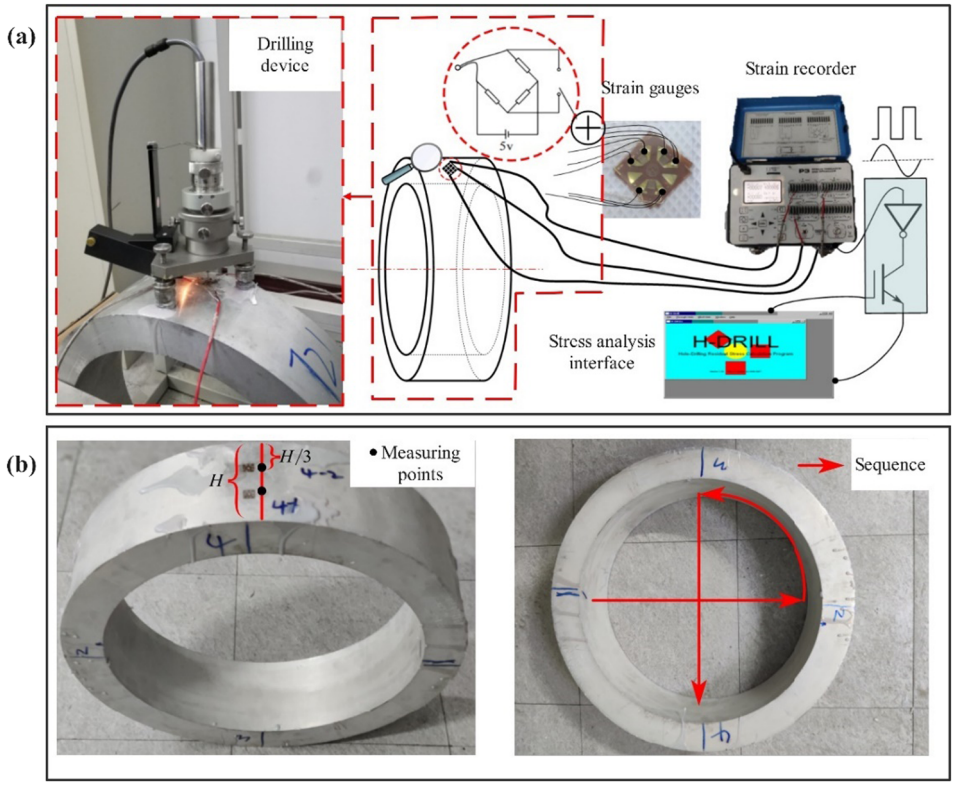

Figure 3: Scheme of (a) residual stress measuring system and (b) measuring points.

tests at four stress levels are shown in Figure 5. The delay function described in equation (3) is chosen to fit the test results for its excellent precision and flexibility.

$$\sigma = \sigma_{\infty} + a_1 e^{-t/b_1} + a_2 e^{-t/b_2} + \cdots + a_{n-1} e^{-t/b_{n-1}} + a_n e^{-t/b_n}, \quad (3)$$

where σ is the instantaneous stress, t is the time, σ_{∞} is the remaining stress after stress relaxation, and a_1–a_n and b_1–b_n are constants determined based on the tests, and the results are shown in Table 2. According to four stress relaxation curve equations, the creep parameters C_1–C_4 of the Norton creep model can be solved, and the results are $C_1 = 1.1518 \times 10^{-12}$, $C_2 = 3.40$, $C_3 = 0.14$, and $C_4 = 409.75$.

In addition, the simulations of TVSR are thermomechanical coupled. The thermophysical parameters used in the simulations are shown in Figure 6.

2.3 TVSR processes optimization

Process parameters determine the effect of TVSR. In order to identify the key factors of TVSR and determine the best process parameters, based on the establishment of the simulation model, this section optimizes the parameters of TVSR. As shown in Figure 7, the maximum equivalent stress after TVSR is the optimization objective, six parameters (heating time, vibration time, vibration amplitude, vibration frequency, holding time, and cooling time) in the heating, vibration, holding, and cooling processes of the TVSR are selected for optimization. The modeling process of TVSR in Section 2.2 is parameterized, element data, material data, load data, and boundary data are constant inputs, while the six selected parameters are stored in parameter data as variables. The TVSR simulation models of different variables are solved cyclically, the maximum equivalent stress is extracted from the result file for evaluating the effect of TVSR.

In the optimization process of TVSR, a uniform sampling method is used to select three values for each parameter in the design space. The optimization process is very slow due to too many (6^3) parameter combinations. In order to improve efficiency, the orthogonal arrays method is used for test design, and the six-factor three-level orthogonal table $L_{27}(3^6)$ is used to combine the parameters. Orthogonal tests of process parameters of TVSR are shown in Table 3.

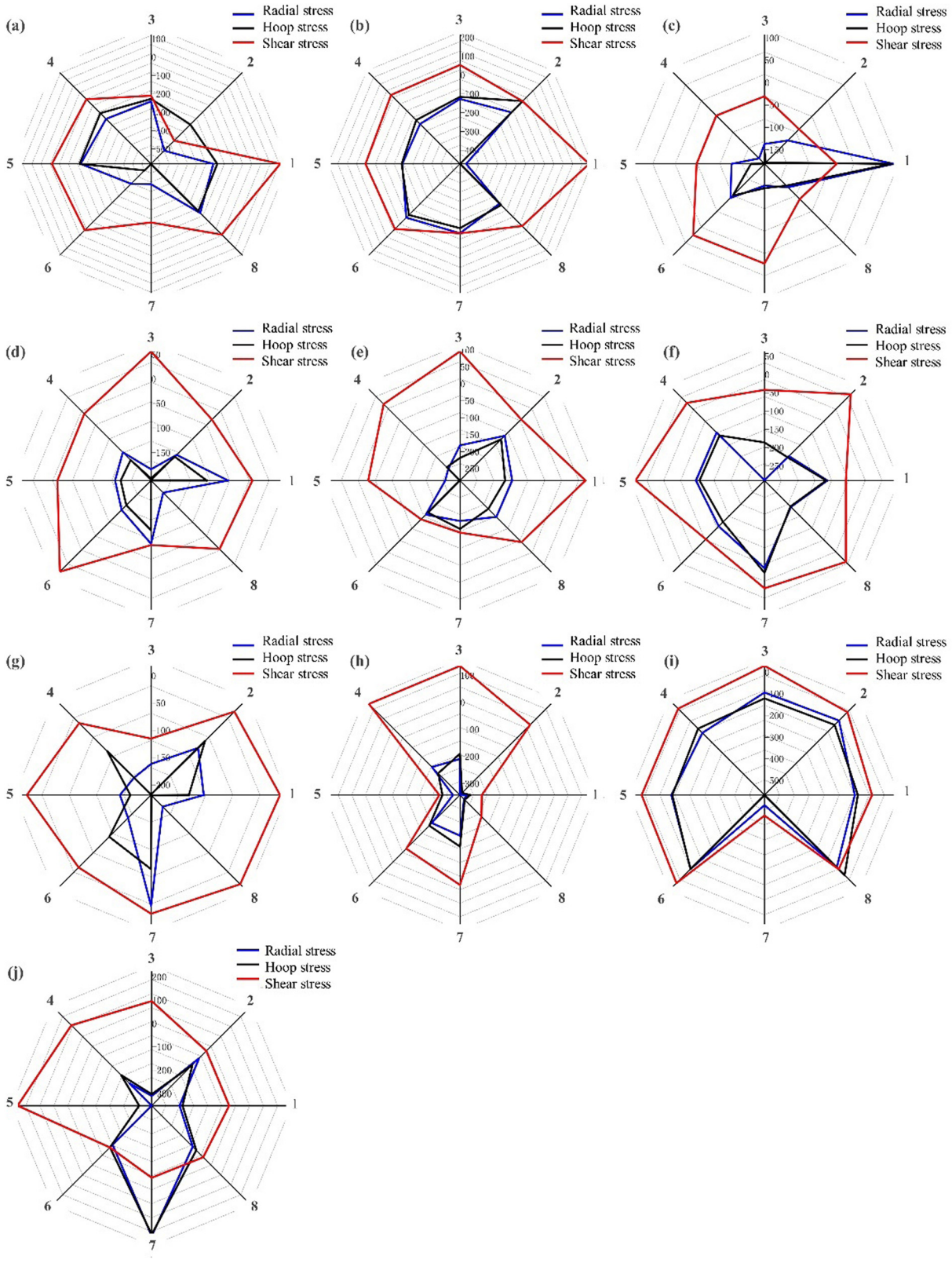

Figure 4: Residual stress at different depths: (a) 0.1 mm; (b) 0.2 mm; (c) 0.3 mm; (d) 0.4 mm; (e) 0.5 mm; (f) 0.6 mm; (g) 0.7 mm; (h) 0.8 mm; (i) 0.9 mm, and (j) 1.0 mm.

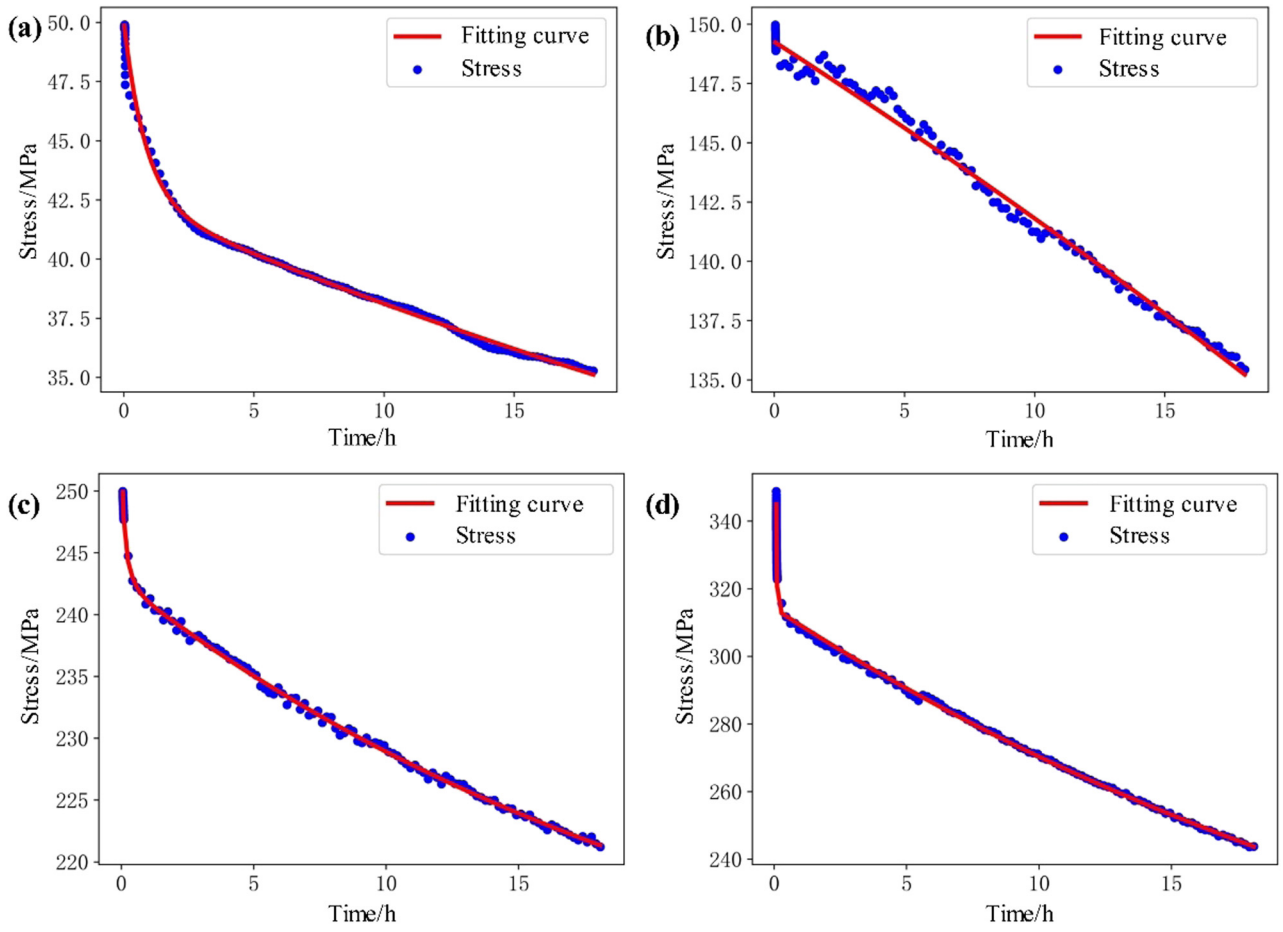

Figure 5: Stress relaxation curves of 2219 aluminum alloy at 175°C under (a) 50 MPa; (b) 150 MPa; (c) 250 MPa; and (d) 350 MPa.

2.4 Rapid prediction based on genetically optimized neural networks

In order to quickly evaluate the TVSR effect of the 2219 aluminum alloy ring, the intelligent optimization prediction algorithm is adopted in this article. Artificial Neural Networks are widely used due to their high computing speed, strong adaptability and fault tolerance, and self-organization ability. However, the training of neural networks is prone to fall into local optimum and prolong the convergence time. Genetic algorithm has a strong adaptive global optimization search ability, which is particularly effective for solving high-dimensional undifferentiable and discontinuous problems. The genetic optimization neural network, which is composed of the two algorithms to avoid their inherent shortcomings, is more accurate and effective.

The structure of the TVSR effect prediction model based on genetically optimized neural networks is shown in Figure 8. First, the neural network structure design for

Table 2: Curve fitting results of stress relaxation of 2219 aluminum alloy

Stress (MPa)	Parameters						
	σ_∞	a_1	b_1	a_2	b_2	a_3	b_3
50	15.859	13.841	55.640	12.801	55.641	7.487	0.832
150	220.261	−23.666	−100.164	−23.669	−100.164	−23.667	−100.164
250	202.553	5.541	0.263	40.062	23.894	10.292	0.045
350	154.149	1096.787	0.022	160.053	31.214	—	—

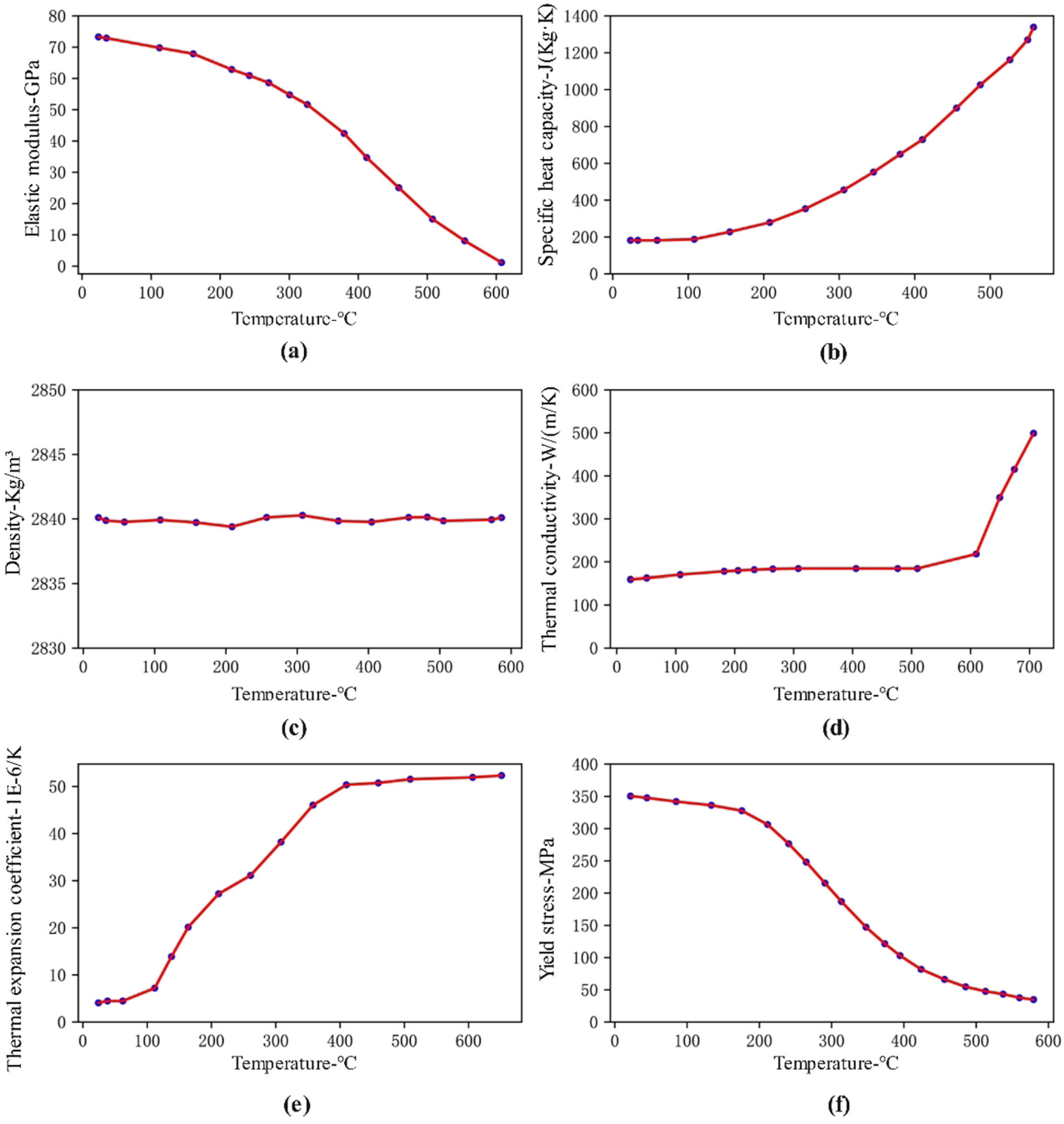

Figure 6: Thermophysical parameters of 2219 aluminum alloy [38–40]: (a) elastic modulus; (b) specific heat capacity; (c) density; (d) thermal conductivity; (e) thermal expansion coefficient; (f) yield stress.

TVSR effect prediction is carried out. The six parameters that affect TVSR are used as input, and the maximum displacement and maximum stress are used as output. Therefore, the number of nodes in the input layer and output layer are six and two respectively. The number of hidden layers selected is two, and the number of neurons is eight. The prediction error of the artificial neural network is defined by the loss function:

$$\min_{w,b\in\Omega} f(w, b) = \sum_{i=1}^{n} |y_i - o_i(w, b)|^2, \tag{4}$$

where n is the total number of training samples, w and b represent the neural network weight and threshold, respectively, Ω is the range of neural network weights and thresholds, y_i is the simulation calculated value of the ith sample, and o_i is the predicted value of the ith sample.

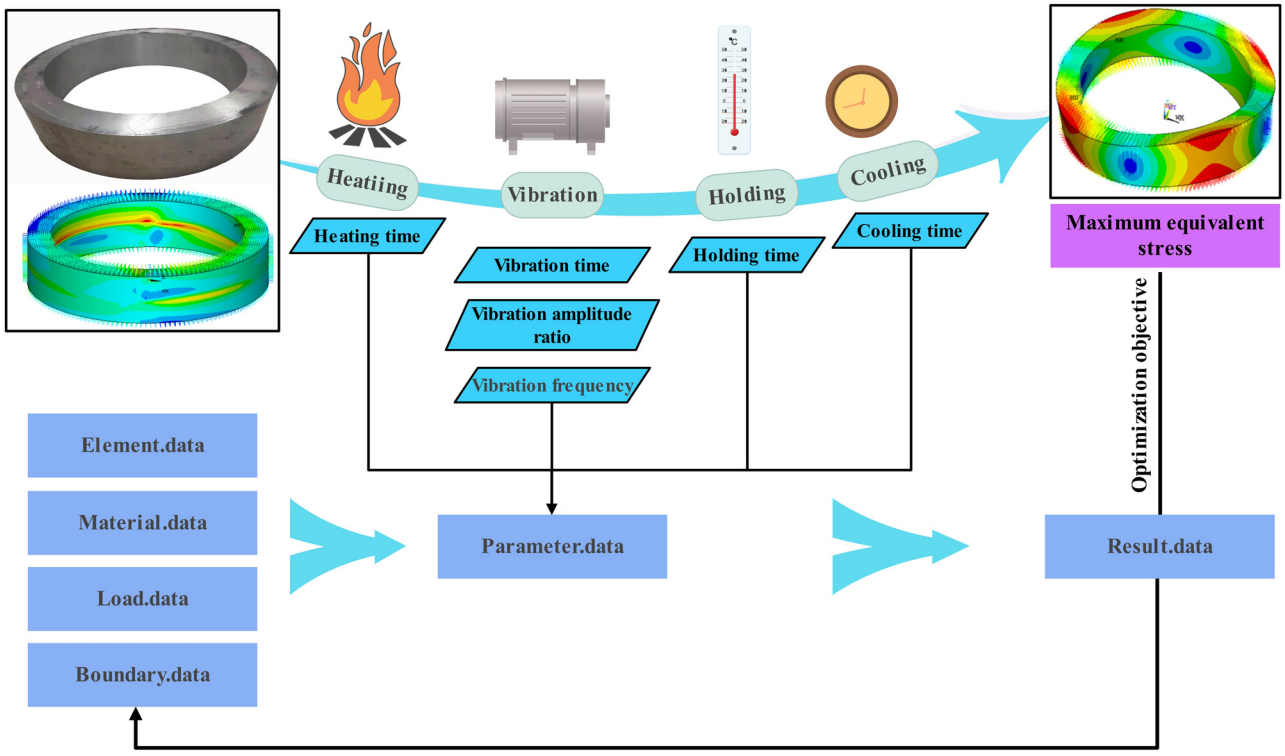

Figure 7: Optimization design process of TVSR parameters.

In order to minimize the loss function, the weights and thresholds are optimized by genetic algorithm. The weight value matrix from the input layer to the first hidden layer is W_1, the threshold matrix of the first hidden layer is B_1, the weight value matrix from the first hidden layer to the second hidden layer is W_2, the threshold matrix of the second hidden layer is B_2, the weight value matrix from the second hidden layer to the output layer is W_3, and the threshold matrix of the output layer is B_3. W_1, B_1, W_2, B_2, W_3, and B_3 are encoded and the initial population of genetically optimized neural networks is obtained. The minimum mean absolute error of the maximum equivalent stress between simulation and genetically optimized neural networks is used as a target for performing the optimization calculations. The mean absolute error is described as equation (5).

$$\mathrm{MEA}(y, \hat{y}) = \frac{1}{m}\sum_{i=1}^{m}|y_i - \hat{y}_i|, \tag{5}$$

where y_i is the ith actual output in the training set, $\hat{y}_i$ is the ith predicted output in the training set, and m is the number of training set samples.

3 Results and discussion

3.1 The influence of TVSR process parameters

According to the TVSR process parameters in Table 3, multiple solutions are obtained, and the solution results are shown in Table 4. The orthogonal test table cannot be directly compared between the groups. In order to identify the key parameters of TVSR, range analysis and gray correlation analysis are used to examine the correlation between the indicators.

The results of range analysis are shown in Table 5. K_i and k_i (i = 1, 2, and 3) are the sum and average of the indicators at the ith level of a certain factor, the range R is the difference between the maximum value $k_{\max}$ and the minimum value $k_{\min}$. It can be found that the vibration amplitude ratio, vibration time, vibration frequency, heating time, holding time, and cooling time all have an impact on the effect of TVSR. With the increase in vibration time, heating time, holding time, and cooling time,

Table 3: Orthogonal test of process parameters of TVSR

	Vibration amplitude ratio	Vibration time (min)	Vibration frequency (Hz)	Heating time (h)	Holding time (h)	Cooling time (h)
1	1	2	619.321	0.5	1	1
2	1	5	619.321	1	1.5	2
3	1	10	619.321	1.5	2	3
4	1	10	982.105	1	1.5	1
5	1	2	982.105	1.5	2	2
6	1	5	982.105	0.5	1	3
7	1	5	1702.953	1.5	2	1
8	1	10	1702.953	0.5	1	2
9	1	2	1702.953	1	1.5	3
10	2	5	619.321	1	2	1
11	2	10	619.321	1.5	1	2
12	2	2	619.321	0.5	1.5	3
13	2	2	982.105	1.5	1	1
14	2	5	982.105	0.5	1.5	2
15	2	10	982.105	1	2	3
16	2	10	1702.953	0.5	1.5	1
17	2	2	1702.953	1	2	2
18	2	5	1702.953	1.5	1	3
19	3	10	619.321	1.5	1.5	1
20	3	2	619.321	0.5	2	2
21	3	5	619.321	1	1	3
22	3	5	982.105	0.5	2	1
23	3	10	982.105	1	1	2
24	3	2	982.105	1.5	1.5	3
25	3	2	1702.953	1	1	1
26	3	5	1702.953	1.5	1.5	2
27	3	10	1702.953	0.5	2	3

the maximum equivalent stress of 2219 aluminum alloy ring after TVSR decreases. However, the increase in the vibration amplitude ratio results in an increase in the maximum equivalent stress. The variation range of R reflects the influence of each parameter on the maximum equivalent stress. The greater the R value, the greater the influence of the parameter. The influence of the TVSR process parameters on the maximum equivalent stress from strong to weak is: vibration frequency > cooling time > holding time > vibration amplitude ratio > heating time > vibration time.

The gray correlation analysis result of the orthogonal test of TVSR is shown in Figure 9. A larger grey relational degree represents a greater influence of the parameter on the target. The results show that, overall, thermal-related parameters have a greater influence on the effect of TVSR than vibration-related parameters. The order of the influence of the parameters determined according to the degree of correlation on the maximum equivalent stress of the ring is: holding time > vibration frequency > cooling time > heating time > vibration amplitude ratio > vibration time. Combining the results of range analysis and gray correlation analysis, holding time and vibration frequency are key parameters of TVSR of the ring. Although a larger frequency can better reduce the residual stress of the ring, it also means that the output power of the vibration equipment is greater, resulting in an increase in cost. Therefore, based on the above analysis, vibration amplitude ratio = 1, vibration time = 5 min, vibration frequency = 619.321 Hz, heating time = 1 h, holding time = 1 h, cooling time = 2 h are preferred TVSR process parameters.

3.2 Prediction results based on genetically optimized neural networks

The simulation results of orthogonal test of TVSR process parameters are used as samples to conduct supervised training on genetically optimized neural networks. The mean absolute error of the maximum equivalent stress during the training process is shown in Figure 10. The mean absolute error is about 0.32 at the beginning, as the number of training increases, the error of the genetically

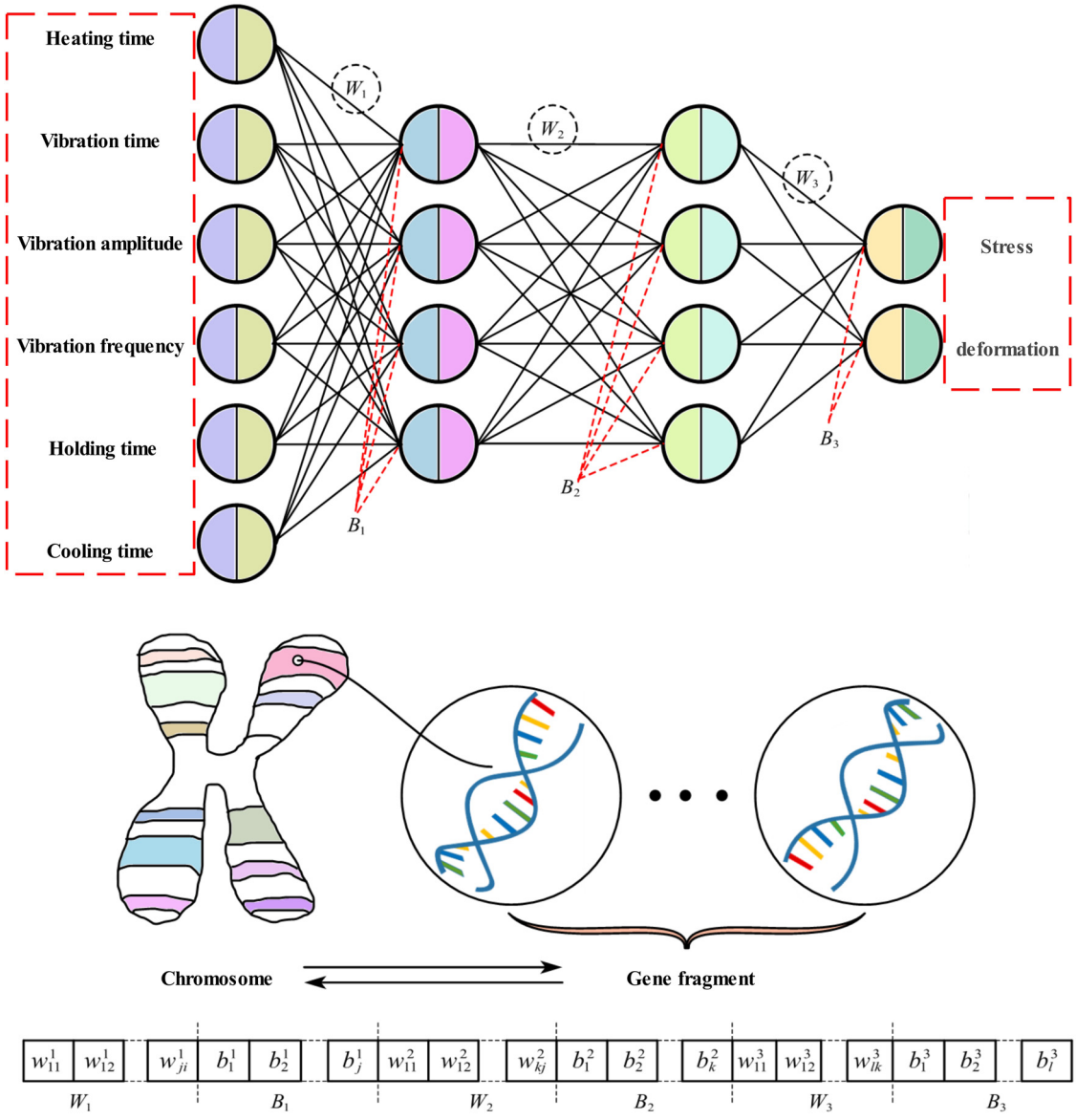

Figure 8: The structure of the TVSR effect prediction model based on genetically optimized neural networks.

Table 4: The simulation results of orthogonal test of TVSR process parameters

	1	2	3	4	5	6	7	8	9
Maximum equivalent stress (MPa)	27.47	21.72	20.88	69.86	61.92	63.60	24.05	26.80	21.48
Stress relief rate (%)	92.6	91.8	93.4	93.3	93.3	93.4	76.6	78.8	80.3
	10	**11**	**12**	**13**	**14**	**15**	**16**	**17**	**18**
Maximum equivalent stress (MPa)	21.77	21.78	21.64	76.20	69.15	64.13	22.56	21.66	21.43
Stress relief rate (%)	93.1	93.4	93.4	93.4	93.3	93.3	78.1	77.3	79.4
	19	**20**	**21**	**22**	**23**	**24**	**25**	**26**	**27**
Maximum equivalent stress (MPa)	21.44	21.77	21.73	71.59	73.94	67.07	26.24	27.71	21.18
Stress relief rate (%)	92.0	91.5	93.5	78.1	77.3	79.4	92.0	91.5	93.5

Table 5: Results of maximum equivalent stress range analysis

	Vibration amplitude ratio	Vibration time (min)	Vibration frequency (Hz)	Heating time (h)	Holding time (h)	Cooling time (h)
K_1	337.7707772	345.4555830	200.2074626	345.7482561	359.1812595	361.1780468
K_2	340.3225238	342.7363319	617.4440205	342.5349137	342.6253943	346.4371340
K_3	352.6591030	342.5604891	213.1009208	342.4692342	328.9457502	323.1372233
k_1	112.5902591	115.1518610	66.7358209	115.2494187	119.7270865	120.3926823
k_2	113.4408413	114.2454440	205.8146735	114.1783046	114.2084648	115.4790447
k_3	117.5530343	114.1868297	71.0336403	114.1564114	109.6485834	107.7124078
R	4.9627753	0.9650313	139.0788526	1.093007	10.0785031	12.6802745

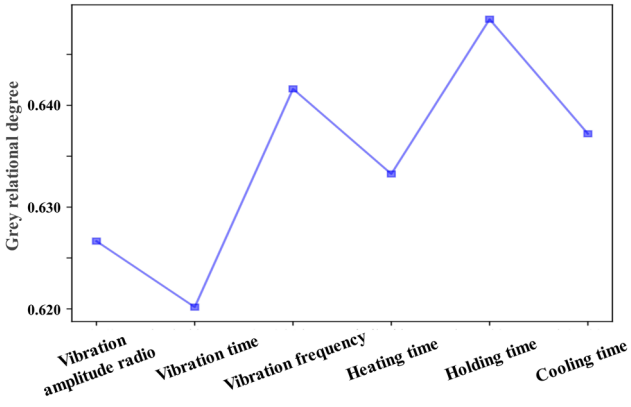

Figure 9: Gray correlation degree of maximum equivalent stress.

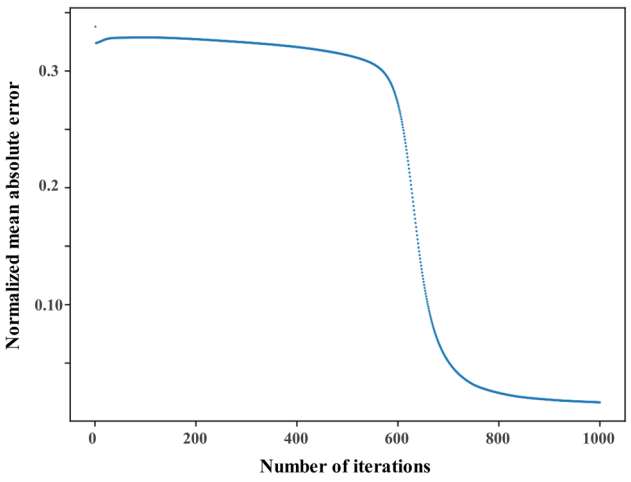

Figure 10: Result of average absolute error.

optimized neural networks decreases rapidly. After 970 trainings, the error decreases to 0.016, indicating that the neural network can basically be used to quickly predict the maximum equivalent stress of the ring after TVSR.

In order to verify the accuracy of the established prediction model based on genetically optimized neural networks, 12 sets of numerical models, which are different

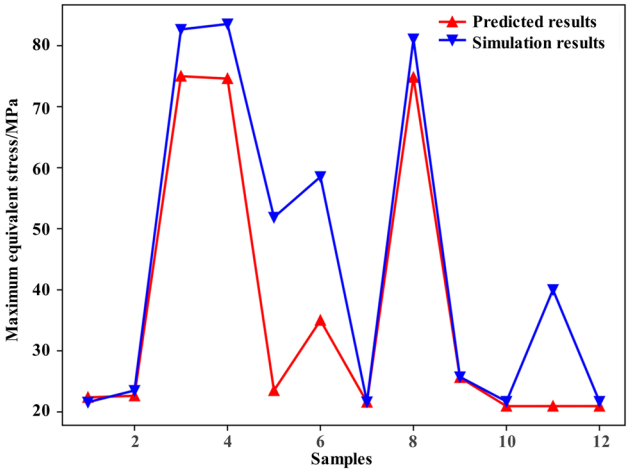

Figure 11: Maximum equivalent stress results of simulation and prediction.

from the TVSR parameters in the orthogonal test, are solved. The result is shown in Figure 11. It can be found that the maximum error is about 25 MPa, which is acceptable compared to the larger initial residual stress (up to −500 MPa) of the 2219 aluminum alloy ring. Moreover, if the number of samples is further increased, the prediction accuracy will be predictably higher.

4 Conclusion

In this study, process optimization of roll formed 2219 aluminum alloy rings is conducted. The influence of vibration amplitude, vibration time, vibration frequency, heating time, holding time, and cooling time on TVSR treatment are investigated. In addition, a genetically optimized artificial neural network intelligent optimization algorithm is applied to quickly predict the TVSR effect of the 2219 aluminum alloy rings. Results can be summarized as:

1. Different TVSR parameters will reduce the different residual stresses of the rings. The maximum equivalent residual stress of the 2219 aluminum alloy rings can be reduced by at least 76.6% after TVSR, and the maximum reduction rate is 93.6%.
2. With the increase in vibration time, heating time, holding time, and cooling time, the maximum equivalent stress of 2219 aluminum alloy rings after TVSR decreases. However, the increase in the vibration amplitude ratio results in an increase in the maximum equivalent stress.
3. Holding time and vibration frequency are key parameters of TVSR of the 2219 aluminum alloy rings.
4. A genetically optimized neural network can be used to quickly predict the effect of TVSR treatment of the 2219 aluminum alloy rings.

Acknowledgment: We acknowledge financial supports from the National Natural Science Foundation of China (52005018), and Defense Industrial Technology Development Program (JCKY2020601C004).

Funding information: The research has been founded by the National Natural Science Foundation of China (52005018) and the Defense Industrial Technology Development Program (JCKY2020601C004).

Author contributions: Shuguang Chen: writing, editing, visualization, methodology, and formal analysis; Hanjun Gao: data curation, editing supervision, discussion, project administration, and funding acquisition; Minghui Lin: experiment; Shaofeng Wu: writing – original draft, conceptualization, formal analysis, visualization, and data curation; Qiong Wu: editing supervision, project administration, and funding acquisition; all authors have discussed and agreed to the published version of the manuscript.

Conflict of interest: Authors state no conflict of interest.

Data availability statement: The data used to support the findings of this study are available from the corresponding author upon request.

References

[1] Liu, H., Y. Chen, and J. Feng. Effect of heat treatment on tensile properties of friction stir welded joints of 2219-T6 aluminium alloy. *Materials Science and Technology*, Vol. 22, No. 2, 2006, pp. 237–241.

[2] Xu, W., J. Liu, G. Luan, and C. Dong. Temperature evolution, microstructure and mechanical properties of friction stir welded thick 2219-O aluminum alloy joints. *Materials & Design*, Vol. 30, No. 6, 2009, pp. 1886–1893.

[3] An, L., Y. Cai, W. Liu, S. Yuan, S. Zhu, and F. Meng. Effect of pre-deformation on microstructure and mechanical properties of 2219 aluminum alloy sheet by thermomechanical treatment. *Transactions of Nonferrous Metals Society of China*, Vol. 22, No. 2, 2012, pp. S370–S375.

[4] Wang, Q., Y. Zhao, T. Zhao, D. Yan, G. Wang, and A. Wu. Influence of restraint conditions on residual stress and distortion of 2219-T8 aluminum alloy TIG welded joints based on contour method. *Journal of Manufacturing Processes*, Vol. 68, 2021, pp. 796–806.

[5] Narayana, G. V., V. M. J. Sharma, V. Diwakar, K. S. Kumar, and R. C. Prasad. Fracture behaviour of aluminium alloy 2219–T87 welded plates. *Science and Technology of Welding and Joining*, Vol. 9, No. 2, 2004, pp. 121–130.

[6] Mao, X., Y. Yi, S. Huang, W. Guo, H. He, and J. Que. Effects of warm saddle forging deformation on the reduction of second-phase particles and control of the three-dimensional mechanical properties of 2219 aluminum alloy rings. *Materials Science and Engineering A – Structural Materials: Properties, Microstructure and Processing*, Vol. 804, 2021, id. 140737.

[7] Guo, W., Y. Yi, S. Huang, X. Mao, J. Fang, D. Tong, et al. Manufacturing large 2219 Al–Cu alloy rings by a cold rolling process. *Materials and Manufacturing Processes*, Vol. 35, No. 3, 2020, pp. 291–302.

[8] Zhang, H., H. Li, G. Zhang, Z. Yin, and L. Wu. Numerical simulation of temperature filed and stress distribution in multi-pass single-layer based rapid prototyping. *6th International Conference on Physical and Numerical Simulation of Materials Processing, Guilin, November 16–19, 2010, Reviews on Advanced Materials Science*, 2013, pp. 402–409.

[9] Chen, S., Q. W. Y. Zhang, H. Gao, Z. Gao, and X. Li. Effect of solid-state phase transformation on residual stress of selective laser melting Ti6Al4V. *Materials Science and Engineering A- Structural Materials: Properties, Microstructure and Processing*, Vol. 819, 2021, id. 141299.

[10] Starke, E. A. and J. T. Staley. Application of modern aluminum alloys to aircraft. *Progress in Aerospace Sciences*, Vol. 32, No. 2, 1996, pp. 131–172.

[11] Heinz, A., A. Haszler, C. Keidel, S. Moldenhauer, R. Benedictus, and W. S. Miller. Recent development in aluminium alloys for aerospace applications. *Materials Science and Engineering A- Structural Materials: Properties, Microstructure and Processing*, Vol. 280, No. 1, 2000, pp. 102–107.

[12] Gao, H., Y. Zhang, Q. Wu, and J. Song. An analytical model for predicting the machining deformation of a plate blank considers biaxial initial residual stresses. *International Journal of Advanced Manufacturing Technology*, Vol. 93, No. 1, 2017, pp. 1473–1486.

[13] Zhu, J. and M. Jia. A new approach for the influence of residual stress on fatigue crack propagation. *Results in Physics*, Vol. 7, 2017, pp. 2204–2212.

[14] Wu, Q., D. Li, and Y. Zhang. Detecting milling deformation in 7075 aluminum alloy aeronautical monolithic components

using the quasi-symmetric machining method. *Metals*, Vol. 6, No. 4, 2016, id. 80.
[15] Gao, H., L. Li, Q. Wu, W. Zhang, G. Dai, and G. Zhang. The optimization of friction disc gear-shaping process aiming at residual stress and machining deformation. *Reviews on Advanced Materials Science*, Vol. 60, No. 1, 2021, pp. 921–935.
[16] Tanner, D. A. and J. S. Robinson. Reducing residual stress in 2014 aluminium alloy die forgings. *Materials & Design*, Vol. 29, No. 7, 2008, pp. 1489–1496.
[17] Williams, R. J., F. Vecchiato, J. Kelleher, M. R. Wenman, P. A. Hooper, and C. M. Davies. Effects of heat treatment on residual stresses in the laser powder bed fusion of 316L stainless steel: Finite element predictions and neutron diffraction measurements. *Journal of Manufacturing Processes*, Vol. 57, 2020, pp. 641–653.
[18] Fredj, N. B. and H. Sidhom. Effects of the cryogenic cooling on the fatigue strength of the AISI 304 stainless steel ground components. *Cryogenics*, Vol. 46, No. 6, 2006, pp. 439–448.
[19] Dong, X., J. Han, D. Ren, K. Mu, Z. Fu, and Y. Zhai. Study on vibratory stress relief of cylindrical welded component with thermal residual stresses. *2nd International Conference on Civil Engineering, Yantai, May 25–27, 2012, Applied Mechanics and Materials*, 2012, pp. 1168–1172.
[20] Zhang, Q., L. Yu, X. Shang, and S. Zhao. Residual stress relief of welded aluminum alloy plate using ultrasonic vibration. *Ultrasonics*, Vol. 107, 2020, id. 106164.
[21] Qu, F., S. Liu, C. Quan, S. Li, and X. Li. Influence of vibratory stress relief on residual stress and mechanical properties of TA15 titanium alloy thick plate. *Heat Treatment of Metals*, Vol. 40, No. 7, 2015, pp. 180–182.
[22] Wang, J. S., C. C. Hsieh, H. H. Lai, C. W. Kuo, P. T. Y. Wu, and W. Wu. The relationships between residual stress relaxation and texture development in AZ31 Mg alloys via the vibratory stress relief technique. *Materials Characterization*, Vol. 99, 2015, pp. 248–253.
[23] Zhang, L. G., G. H. Huo, H. Xiao, H. B. Xie, and Z. Y. He. Numerical simulation of vibration stress relief treatment of 304 stainless steel cold rolled strip. *Iron & Steel*, Vol. 53, No. 1, 2018, pp. 59–64.
[24] Lv, T. and Y. Zhang. A combined method of thermal and vibratory stress relief. *Journal of Vibroengineering*, Vol. 17, No. 6, 2015, pp. 2837–2845.
[25] Chen, S. G., Y. Zhang, Q. Wu, H. Gao, and D. Yan. Residual stress relief for 2219 aluminum alloy weldments: a comparative study on three stress relief methods. *Metals*, Vol. 9, No. 4, 2019, id. 419.
[26] Li, S., H. Fang, X. Liu, and W. Cui. Thermal vibration compound stress relief on thick DH36 steel welded plates. *Applied Mechanics & Materials*, Vol. 576, 2014, pp. 143–147.
[27] Wu, Q., J. Wu, Y. Zhang, H. Gao, and D. Hui. Analysis and homogenization of residual stress in aerospace ring rolling process of 2219 aluminum alloy using thermal stress relief method. *International Journal of Mechanical Sciences*, Vol. 157, 2019, pp. 111–118.
[28] Xu, Y., Z. Shi, B. Li, and Z. Zhang. Effects of TVSR process on the dimensional stability and residual stress of 7075 aluminum alloy parts. *Reviews on Advanced Materials Science*, Vol. 60, No. 1, 2021, pp. 631–642.
[29] Wu, Q., W. Miao, H. Gao, Y. Zhang, D. Xie, and M. Yang. Residual stress homogenization of SiCP/Al composites with thermal vibration coupling. *International Journal of Advanced Manufacturing Technology*, Vol. 112, No. 5, 2021, pp. 1691–1703.
[30] Gao, H., S. Wu, Q. Wu, B. Li, Z. Gao, Y. Zhang, et al. Experimental and simulation investigation on thermal-vibratory stress relief process for 7075 aluminium alloy. *Materials & Design*, Vol. 195, 2020, id. 108954.
[31] Baere, D. D., P. V. Cauwenbergh, M. Bayat, S. Mohanty, J. Thorborg, L. Thijs, et al. Thermo-mechanical modelling of stress relief heat treatments after laser-based powder bed fusion. *Additive Manufacturing*, Vol. 38, 2021, id. 101818.
[32] Chen, J., J. Jiang, L. Zhen, and W. Shao. Stress relaxation behavior of an Al–Zn–Mg–Cu alloy in simulated age-forming process. *Journal of Materials Processing Technology*, Vol. 214, No. 4, 2014, pp. 775–783.
[33] Shen, W. F., C. Zhang, L. Zhang, Y. Yang, and Z. Zhu. Stress relaxation behaviour and creep constitutive equations of SA302Gr.C low-alloy steel. *High Temperature Materials and Processes*, Vol. 37, No. 9, 2018, pp. 857–862.
[34] Cai, Y. X., L. Zhan, Y. Xu, C. Liu, J. Wang, X. Zhao, et al. Stress relaxation aging behavior and constitutive modelling of AA7150-T7751 under different temperatures, initial stress levels and pre-strains. *Metals*, Vol. 9, No. 11, 2019, id. 1215.
[35] Godlewski, L. A., X. Su, T. M. Pollock, and J. E. Allison. The effect of aging on the relaxation of residual stress in cast aluminum. *Metallurgical and Materials Transactions A – Physical metallurgy and materials science*, Vol. 44A, No. 10, 2013, pp. 4809–4818.
[36] Zheng, J., J. Lin, J. Lee, R. Pan, C. Li, and C. M. Davies. A novel constitutive model for multi-step stress relaxation ageing of a pre-strained 7xxx series alloy. *International Journal of Plasticity*, Vol. 106, 2018, pp. 31–47.
[37] Zhou, J., X. Zhang, and J. Wang. FEM simulation of stress relaxation age forming for AA7055 thin plate. *Ordnance Material Science and Engineering*, Vol. 36, No. 3, 2013, pp. 98–101.
[38] Ma, Y., N. Xue, Q. Wu, H. Gao, and J. Wu. Residual stress analysis of a 2219 aluminum alloy ring using the indentation strain-gauge method. *Metals*, Vol. 10, No. 7, 2020, id. 979.
[39] Ahmad, A. S., Y. Wu, H. Gong, and L. Liu. Determination of the effect of cold working compression on residual stress reduction in quenched aluminum alloy 2219 block. *Strojniski Vestnik-Journal of Mechanical Engineering*, Vol. 65, No. 5, 2019, pp. 311–318.
[40] Ahmad, A. S., Y. Wu, H. Gong, and L. Liu. Numerical simulation of thermal and residual stress field induced by three-pass TIG welding of Al 2219 considering the effect of interpass cooling. *International Journal of Precision Engineering and Manufacturing*, Vol. 21, No. 8, 2020, pp. 1501–1518.